Electronic structure of Co 3d states in the Kitaev material candidate honeycomb cobaltate Na₃Co₂SbO₆ probed with x-ray dichroism

M. van Veenendaal [1,2,*] E. H. T. Poldi [3,2] L. S. I. Veiga,[4] P. Bencok,[4] G. Fabbris [2] R. Tartaglia,[5,2] J. L. McChesney [2]
J. W. Freeland,[2] R. J. Hemley,[6] H. Zheng,[7] J. F. Mitchell [7] J.-Q. Yan [8] and D. Haskel [2,†]

[1]*Department of Physics, Northern Illinois University, DeKalb, Illinois 60115, USA*
[2]*Advanced Photon Source, Argonne National Laboratory, Argonne, Illinois 60439, USA*
[3]*Department of Physics, University of Illinois Chicago, Chicago, Illinois 60607, USA*
[4]*Diamond Light Source Ltd., Harwell Science and Innovation Campus, Didcot, Oxfordshire OX11 0DE, United Kingdom*
[5]*Gleb Wataghin Institute of Physics, University of Campinas-UNICAMP, São Paulo 13083-859, Brazil*
[6]*Departments of Physics, Chemistry, and Earth and Environmental Sciences, University of Illinois Chicago, Chicago, Illinois 60607, USA*
[7]*Materials Science Division, Argonne National Laboratory, Argonne, Illinois 60439, USA*
[8]*Materials Science and Technology Division, Oak Ridge National Laboratory, Oak Ridge, Tennessee 37831, USA*

The recent prediction that honeycomb lattices of Co^{2+} ($3d^7$) ions could host dominant Kitaev interactions provides an exciting direction for exploration of new routes to stabilizing Kitaev's quantum spin liquid in real materials. $Na_3Co_2SbO_6$ has been singled out as a potential material candidate provided that spin and orbital moments couple into a $J_{eff} = \frac{1}{2}$ ground state, and that the relative strength of trigonal crystal field and spin-orbit coupling acting on Co ions can be tailored. Using x-ray linear dichroism (XLD) and x-ray magnetic circular dichroism (XMCD) experiments, alongside configuration interaction calculations, we confirm the counterintuitive positive sign of the trigonal crystal field acting on Co^{2+} ions and test the validity of the $J_{eff} = \frac{1}{2}$ description of the electronic ground state. The results lend experimental support to recent theoretical predictions that a compression (elongation) of CoO_6 octahedra along (perpendicular to) the trigonal axis would drive this cobaltate toward the Kitaev limit, assuming the $J_{eff} = \frac{1}{2}$ character of the electronic ground state is preserved.

I. INTRODUCTION

Since the prediction by Kitaev that 2D honeycomb spin lattices with bond-dependent, Ising-like ferromagnetic interactions can host a quantum spin liquid (QSL) ground state with topologically protected fractionalized excitations [1], a flurry of activity has ensued aimed at realizing the Kitaev model in real materials [2,3]. Much of the search so far has focused on honeycomb lattices of ruthenates [4–9], rhodates [10–12], and iridates [13–17], where Ru^{3+}, Rh^{4+}, and Ir^{4+} ions in octahedral coordination adopt a t_{2g} d^5 low-spin configuration. The strong spin-orbit interaction in heavy $4d/5d$ ions leads to emergence of $j_{eff} = \frac{1}{2}$ "pseudospin" magnetic moments within the t_{2g} manifold with entangled spin and orbital moments [18,19]. A perfect honeycomb lattice of pseudospins in regular, edge-shared octahedra is predicted to result in vanishing first neighbor isotropic Heisenberg superexchange interactions and, in the absence of sizable longer range or direct exchange interactions, a dominant Kitaev exchange interaction between pseudospins [20]. Experimentally, however, lattice distortions prevent realization of regular octahedra or perfect honeycomb lattices, and isotropic exchange interactions are found to coexist alongside the frustrated,

bond-dependent Kitaev exchange interactions, resulting in magnetically ordered ground states [21–26]. Attempts to drive ruthenate, rhodate, and iridate honeycombs toward Kitaev's QSL state with chemical doping [27–31] or application of external pressure [32–38] have faced challenges, including phase separation and formation of glassy phases with doping, and a tendency of closely spaced Ru/Rh $4d$ or Ir $5d$ orbitals across edge-shared octahedra to dimerize, especially under pressure, a result of spatially extended $4d/5d$ orbitals. This dimerization leads to a collapse of the $j_{eff} = \frac{1}{2}$ pseudospins [39,40], which are otherwise required to map the exchange interactions into Kitaev's model, and to the emergence of molecular orbitals with spin pairs locked into nonmagnetic singlets [40–42] preventing realization of the dynamic QSL state.

A new paradigm has recently emerged with the proposal that honeycomb lattices of Co^{2+} $3d^7$ ions can serve as a new platform to search for Kitaev's QSL [43–45]. The high-spin Co^{2+} ions can also have a pseudospin $J_{eff} = \frac{1}{2}$ ground state in the presence of spin-orbit interactions ($S = \frac{3}{2}$, $L_{eff} = 1$) (note: we use J_{eff} notation for many-body states and j_{eff} for single-particle states). Unlike exchange interactions in low-spin d^5 ruthenates, rhodates, and iridates, which only involve t_{2g}-t_{2g} exchange pathways, the high-spin $3d^7$ configuration of Co^{2+} ions results in additional t_{2g}-e_g and e_g-e_g exchange channels [43,45]. It was demonstrated that these additional exchange pathways contribute with nearly equal magnitude but

*veenendaal@niu.edu
†haskel@anl.gov

214443-1

opposite sign to the isotropic Heisenberg exchange, which nearly cancels, resulting in dominant Kitaev exchange interactions arising from within the t_{2g}-e_g exchange channel [43]. Since the spatial extent of $3d$ orbitals is much reduced relative to that of $4d$ and $5d$ counterparts, the honeycomb cobaltates are more robust against dimerization of $3d$ orbitals across edge-shared octahedra. In addition, the reduced radial extent of $3d$ orbitals aids in confining magnetic interactions to nearest neighbours and in suppressing direct exchange between Co ions across edge-shared octahedra. Stabilization of Kitaev's QSL in a honeycomb cobaltate would open the door to a whole new class of materials that could host such states, circumventing the limitations present in $4d$ and $5d$ honeycombs.

$Na_3Co_2SbO_6$ is one such candidate material to host a Kitaev QSL [43]. While it orders magnetically with a zigzag structure below $T_N \sim 5$–8 K [46–49], theoretical predictions suggest that a Kitaev QSL can be stabilized in this material if the *positive* trigonal crystal field acting on Co^{2+} ions can be reduced by about 20 meV [43]. A positive sign of trigonal crystal field seems counterintuitive since the CoO_6 octahedra are compressed along their trigonal axis, which corresponds to a *negative* trigonal crystal field when only accounting for the electric field generated by oxygen charges in octahedral cages [43,50–52]. The positive sign of trigonal crystal field was derived from analysis of magnetic susceptibility data, and a point charge model used to attribute the inverted sign to the contribution of charges in Sb^{5+} ions located in the honeycomb layers [43]. A positive sign of trigonal crystal field was also deduced from modeling of crystal field excitations probed with inelastic neutron scattering [53].

Considering the convoluted contributions to the trigonal field, it is important to provide additional experimental validation for the sign of the trigonal crystal field acting on Co^{2+} ions in order to guide experimental work aimed at driving this system toward the QSL state by manipulating the ratio of trigonal crystal field, Δ, to spin-orbit interaction, ζ, along the line of theoretical predictions [43]. If the net trigonal crystal field is positive, further *compression* of CoO_6 octahedra along their trigonal axis (a more negative contribution to the trigonal field) will reduce $|\Delta/\zeta|$. If the net trigonal crystal field is negative, an *expansion* of the CoO_6 octahedra along their trigonal axis (a positive contribution to the trigonal field) will reduce $|\Delta/\zeta|$. Corroboration of the sign of the trigonal crystal field will hence aid in the design of experiments aimed at using hydrostatic pressure or uniaxial strain to properly tune $|\Delta|$ toward stabilization of Kitaev's QSL state.

The exact nature of the spin-orbit entangled pseudospin $J_{\text{eff}} = \frac{1}{2}$ wave function of Co^{2+} ions depends on Δ/ζ, as nonzero values of Δ tend to quench orbital angular momentum [43]. The related modification to the spin-orbital exchange interactions dictates the relative contributions of Kitaev (K), Heisenberg (J), and off-diagonal anisotropic (Γ, Γ') exchange to the microscopic Hamiltonian. Not surprisingly, the anisotropic K, Γ, Γ' interactions are shown to have the strongest dependence on Δ [43]. Since the magnitude of non-Kitaev spin-orbital exchange interactions is intimately tied to the nature of the J_{eff} pseudospin wave function (via Δ/ζ), it is important to provide experimental validation of the $J_{\text{eff}} = \frac{1}{2}$ description of the $3d$ electronic ground state. The observation of spin-orbit excitations between $J_{\text{eff}} = \frac{1}{2}$

and $J_{\text{eff}} = \frac{3}{2}$ states in recent inelastic neutron scattering studies [53,54] appears to validate the presence of a spin-orbit entangled $J_{\text{eff}} = \frac{1}{2}$ ground state in $Na_3Co_2SbO_6$ despite the much reduced spin-orbit interaction in $3d$ orbitals relative to their $4d$, $5d$ counterparts.

Here we present x-ray absorption spectroscopy (XAS), x-ray magnetic circular dichroism (XMCD), and x-ray linear dichroism (XLD) measurements at the Co $L_{2,3}$ edges in $Na_3Co_2SbO_6$, alongside their theoretical modeling and interpretation, to shed light onto the sign of the trigonal distortion and the validity of the $J_{\text{eff}} = \frac{1}{2}$ description of the ground state. XAS and XMCD provide a nexus to test the validity of the $J_{\text{eff}} = \frac{1}{2}$ description of the electronic ground state. XAS at spin-orbit split core levels such as the Co $L_{2,3}$ absorption edges is sensitive to the expectation value of the angular part of the spin-orbit interaction in the Co $3d$ states, via the isotropic branching ratio [55,56]. Additionally, XMCD is sensitive to both orbital and spin moments in Co $3d$ orbitals [57,58]. XLD measures the anisotropic $3d$ orbital occupation [59], namely, the quadrupole moment in the multipole expansion of the $3d$ charge distribution [60] arising from the combined effects of trigonal crystal field and spin-orbit coupling. In the limit $\zeta \to 0$ a sign inversion of the trigonal crystal field reverses the order of singlet a_{1g} and doublet e'_g states [50–52] affecting the orbital character of the hole in the t_{2g}-derived states.

The paper is organized as follows: Section II includes details on sample preparation together with details on experimental setup and data collection. Section III describes theoretical modeling and numerical computation of XAS, XLD, and XMCD spectra, providing insight into the connection between XLD spectra and quadrupole moments, the nature of the ground state, and derivation of sign and magnitude of trigonal crystal field acting on Co $3d$ orbitals. Section IV summarizes the main findings of the paper. The Appendix contains additional details on data treatments and modeling.

II. EXPERIMENTAL

A. Sample preparation

Polycrystalline powder was used for XMCD measurements while single crystals were used for the XLD measurements. Polycrystalline samples of $Na_3Co_2SbO_6$ were prepared by a solid-state reaction method. Stoichiometric quantities of Co_3O_4 and Sb_2O_3 were combined and thoroughly ground together with a 10% molar excess of Na_2CO_3. The powder mixture was heated to 900 °C at 2 °C/min in a loosely covered platinum crucible, soaked for 24 hours, and then cooled at 3 °C/min. The pink powder was reground and pressed into pellets and heated again at 900 °C for 48 hours on sacrificial powder. The pellets were reground, mixed with a 30 wt % excess Na_2CO_3, again pressed into pellets, and fired at 1100 °C for 48 hours. For this firing, the pellets were placed on an aluminum oxide plate covered with sacrificial powder to avoid the partially melted pellets sticking to the platinum crucible. The pink powders prepared this way were single phase as judged by laboratory powder diffraction. Magnetic susceptibility measurements confirmed antiferromagnetic or-

dering below $T_N = 8$ K. Note that $Na_3Co_2SbO_6$ is moisture sensitive over the long term and should be stored in an inert atmosphere. Single-crystal samples were prepared as described in Ref. [48]. All single-crystal measurements presented here were done on crystals from the same batch.

B. XMCD measurements

The XMCD measurements at the Co $L_{2,3}$ edges were carried out at beamline I10 of the Diamond Light Source (DLS), UK, using total electron yield (TEY) detection. The powder sample was spread onto carbon tape and data collected at $T = 2$ K in a 14 T magnetic field applied along the incident wave vector. Polarization control was provided by the beamline's Apple II undulators. Polarization was fixed during energy scans, and x-ray helicity switched between consecutive scans. Sum rules alongside numerical calculations were used to derive ground-state expectation values of spin and orbital angular momentum, as described in Sec. III F.

C. XLD measurements

XLD measurements at the Co $L_{2,3}$ edges were conducted both at beamline I10 of the DLS and beamline 29-ID-D of the Advanced Photon Source (APS) of Argonne National Laboratory. The XLD measurements at the DLS were conducted in zero applied magnetic field, at $T = 2$–3 K, using total fluorescence yield (TFY) detection. Data were collected on as-grown single crystals mounted on carbon tape. Crystals are platelet-like, hexagonal shaped, with the c axis oriented along the surface normal. No care was taken to align the in-plane crystal orientation (a total of four crystals were measured with random in-plane orientation). Typical single-crystal size was ≈500 μm × 500 μm. The experimental geometry is shown in the inset of Fig. 1. The XLD measurements were done at normal incidence ($\theta = 90°$) and grazing incidence ($\theta = 20°$), where θ is the angle between the incident x-ray wave vector and the surface. The XLD spectrum is defined as the difference between linear vertical (in-plane) and linear horizontal polarizations (horizontal polarization is along crystal c axis for $\theta = 0°$). The grazing incidence geometry probes XLD between in-plane and (nearly) out-of-plane directions; the normal incidence geometry probes in-plane XLD. Polarization was kept fixed to either linear-H or linear-V during energy scans. To compare with numerical calculations, TFY data underwent an *ad hoc* correction for self-absorption based on the observation, from modeling, that the sum of XAS spectra for the two linear polarizations is close to the isotropic XAS spectrum, which is measured undistorted in XMCD-TEY powder measurements. The polarization-averaged XAS spectrum was matched to the undistorted isotropic XAS spectrum, and the XLD data corrected with the same functional form (see Fig. 6 of the Appendix for more details). The dominant effect of the correction is the removal of the suppression of the intensity at the L_3 edge with respect to the L_2 edge.

The XLD measurements at APS were conducted on a single crystal that was cleaved *in situ* in order to expose a fresh surface for TEY detection. Measurements were done in zero applied field, at $T = 150$ K. Polarization control was provided by the beamline's electromagnetic variable polariza-
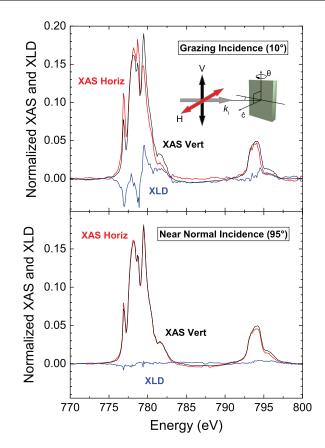

FIG. 1. Polarization-dependent x-ray absorption spectra detected in TEY mode at grazing incidence and near normal incidence angles ($T = 150$ K). The linear dichroism is obtained as the difference in XAS spectra between linear vertical and linear horizontal polarization. The inset in the top panel shows the experimental geometry.

tion undulator. Polarization was kept fixed to either linear-H or linear-V during energy scans. Experimental geometry was the same used at the DLS, with measurements carried out at various incidence angles between $\theta = 0°$ and $\theta = 95°$. The beamline's in-vacuum diffractometer, together with its access to tender x-ray energies (2500 eV), allowed accessing the (001) Bragg reflection to confirm that the crystalline c axis was oriented along the crystal surface normal.

XLD measurements were also carried out at the Co K edge at beamline 4-ID-D of the APS. Switching between linear horizontal and linear vertical polarization was achieved with the use of two in-line C(111) diamond phase plates, each 180 μm in thickness. The first phase plate is set to achieve circular polarization ($\pi/2$ phase shift between orthogonal polarization components) while the second phase plate is alternated between $\pm\pi/2$ conditions to switch between linear polarization states at each energy point during energy scans. A 4-element silicon drift diode energy discriminating detector was used to detect Co K_α emission in partial fluorescence yield mode. Measurements were done in zero magnetic field at 2 K, using the same experimental geometry as in the other XLD measurements.

Sizable XLD is detected between in-plane and out-of-plane directions, as expected for this layered honeycomb structure (Fig. 1). On the other hand, the angular-dependent XLD measurements at both Co $L_{2,3}$ and K edges clearly show
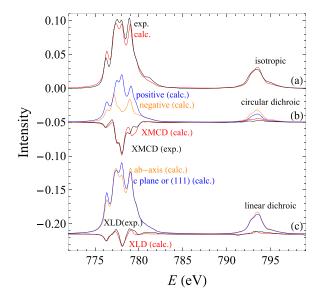
FIG. 2. Comparison between experimental (black) and calculated (red) spectra. (a) The isotropic spectrum, and (b) the XMCD spectrum obtained as the difference of the spectra for negative (orange) and positive (blue) helicity of circularly polarized light. Data are from powder sample at $T = 2$ K, $H = 14$ T. (c) XLD spectrum collected in TFY mode. XLD at incidence angle $\theta = 0$ is the difference of the spectra with polarization in the plane perpendicular to the (111) axis of the CoO_6 octahedra and along the (111) direction. TFY data were collected on single-crystal samples at $T = 2$–3 K in zero applied field, at $\theta = 20°$ incidence angle, and were corrected for self-absorption.

FIG. 3. Modeling of XLD-TFY spectrum for different values of the trigonal crystal field: -35 (blue), 35 (red), and 50 (gray) meV. Note that the XLD signal is, to lowest order, proportional to the strength of the trigonal field and therefore changes sign for an opposite trigonal field. Inset shows structure of CoO_6 honeycomb planes with global (a, b, and c) and local (100, 010, and 001) systems of coordinates highlighted. Octahedra are distorted along the trigonal axis, i.e., local (111) axis, represented by the black arrow.

that XLD signal gradually diminishes when moving toward normal incidence, vanishing when both vertical and horizontal polarizations lie in the honeycomb planes (Fig. 1 and Appendix Figs. 9 and 10). This indicates that the in-plane component of the Co 3d charge distribution is isotropic, and also confirms that the random alignment of in-plane crystal orientation during crystal mounting has no bearing on the results.

We note that the self-absorption corrected XLD data collected in TFY mode at the DLS using as-grown crystals, and the XLD data collected in TEY mode at APS on an *in situ* cleaved crystal, have similar line shapes but display differences in relative amplitudes between peaks (see Fig. 1 and Fig. 3; a more direct comparison is shown in Fig. 6 of the Appendix). Unlike TEY, the TFY signal is a bulk probe, hence less sensitive to surface effects. On the other hand the self-absorption correction of TFY data may introduce distortions in the data. An additional possible source of discrepancy is the different temperatures used in the TFY and TEY measurements (2–3 K versus 150 K). It is worth noting that although the TFY measurements were done at 2–3 K, within the magnetically ordered phase ($T_N = 8$ K), the XLD signal is not of magnetic origin; i.e., it is not x-ray magnetic linear dichroism (XMLD). The data were obtained in zero applied field (zero field cooling) so no field-biasing of AFM domains took place. The horizontal x-ray beam size of $\sim$300 μm ($\sim$1 mm at grazing incidence) is expected to be much larger than, and average over, AFM and twin domains present in this honeycomb monoclinic structure. Most importantly, the zigzag magnetic
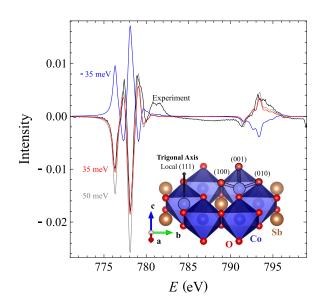
ordering is a collinear antiferromagnetic arrangement of Co moments lying in the honeycomb planes [48]. If the XLD signal were to be of magnetic origin, its dependence on θ will be dramatically different than observation (i.e., negligible angular dependence for AFM domains with in-plane Co moments pointing in the vertical direction, and a much larger XLD signal at normal incidence relative to grazing incidence for AFM domains with in-plane Co moments pointing in the horizontal direction) [61]. Additional evidence that the TFY-XLD signal is not of magnetic origin is a lack of signal dependence on in-plane crystal mounting orientation, and the similar line shape of TEY-XLD measured at 150 K.

We show modeling results for the self-absorption corrected TFY data here in the main paper as these data are bulk sensitive and not influenced by potential surface modifications. The numerical calculations show better agreement with the TFY than the TEY data. However, we also modeled the surface-sensitive TEY data and included those results in the Appendix (Fig. 7). The differences between TFY and TEY data modeling mainly translate into an uncertainty in the size of the derived trigonal crystal field, but do not have bearing on the conclusions regarding the sign of the trigonal crystal field.

III. THEORY AND MODELING

A. Hamiltonian

The spectra are calculated using a Hamiltonian [62–64] including the Coulomb interaction between the 3d electrons, the Coulomb interaction between the 2p and 3d electrons, spin-orbit interactions for the 2p and 3d electrons, and octahedral and trigonal crystal fields. Parameters for the Coulomb interaction are calculated within the Hartree-Fock limit and

scaled down to 70% to account for covalency and inter-atomic screening. The strength of the one-particle spin-orbit interaction $\sum_i \zeta \mathbf{l}_i \cdot \mathbf{s}_i$, where the summation i goes over the electrons, is calculated in the same limit giving a value of $\zeta = 66$ meV. The parameter for the $2p$ spin-orbit interaction is $\zeta_{2p} = 9.75$ eV. The parameters for the crystal fields are adjustable and chosen to obtain the best agreement with the x-ray spectra. The octahedral crystal field is $10Dq = 1.1$ eV. The calculation also includes a trigonal crystal field

$$H_{\text{trig}} = \sum_{\substack{\alpha,\alpha'=xy,yz,zx \\ \alpha \neq \alpha'}} \sum_{\sigma=\pm\frac{1}{2}} \frac{\Delta}{3} c^{\dagger}_{\alpha'\sigma} c_{\alpha\sigma}, \tag{1}$$

where the orbitals are defined with respect to the CoO_6 octahedra. The summation goes over the t_{2g} orbitals with $\alpha = xy, yz, zx$. The eigenenergies of the trigonal field are $\frac{2}{3}\Delta, -\frac{1}{3}\Delta, -\frac{1}{3}\Delta$. For a positive Δ, the holes preferentially go into the state with energy $\frac{2}{3}\Delta$ which has an eigenfunction $|a_1\rangle = (|xy\rangle + |yz\rangle + |zx\rangle)/\sqrt{3}$. However, as we shall see below, in the presence of the Coulomb interaction, octahedral crystal fields, and spin-orbit interactions, the many-body ground state is significantly more complex.

The spectra are fitted within an atomic framework. Due to the absence of clear, core-hole screening satellite features on the high-energy side of the multiplet structure, which otherwise arise from covalent mixing in the final state [64,65], the x-ray absorption spectra of this compound are not well suited for accurate determination of the charge-transfer energy and the on-site repulsion. However, the spectra can be fitted rather well using an atomic model where the effects of the ligands are included by an effective crystal field. This approach follows closely that of Liu *et al.* [43] in their determination of the ground state of divalent cobalt.

B. Spectral line shapes

A comparison between the different polarized spectra is shown in Fig. 2. The calculated isotropic spectrum in Fig. 2(a) agrees well with experiment (powder sample) for the used crystal field [62]. The trigonal field has little effect on the isotropic spectrum. The spectrum shows two clear edges related to the splitting by the $2p$ spin-orbit interaction. Additional fine structure is due to the Coulomb interactions and the octahedral crystal field. Figure 2(b) shows XMCD data for the powder sample. The calculated spectrum is again in satisfactory agreement with experiment.

Figure 2(c) shows the XLD data, which are displayed in greater detail in Fig. 3. The XLD is measured as the difference between spectra with the polarization in the crystallographic *ab* plane and near the *c* axis. Due to experimental limitations, the latter spectrum is taken 20° away from the *c* axis, which also has been taken into account in the calculations. The cobalt ions form a hexagonal lattice in the crystallographic *ab* plane. The CoO_6 octahedra are oriented such that the (111) direction of the octahedra is approximately along the crystallographic *c* axis; see the inset in Fig. 3. The presence of XLD indicates a trigonal distortion since no XLD is expected for octahedral symmetry. The best agreement is obtained for a trigonal crystal field of $\Delta = 35$ meV, leading to an increased hole density in the $|a_1\rangle$ orbital. Figure 3 shows the effect of a change in

trigonal field on the XLD. Apart from small details, the XLD for small Δ simply scales with the trigonal field. Most notably, the sign of the XLD reverses when changing the sign of Δ. In the following, we look in more detail at how the magnitude and trends of the linear dichroism can be directly related to ground-state properties and the size of the trigonal field.

C. Quadrupole moments

There are different ways that a change in parameters can affect the spectral line shape. Obviously, for a large parameter the spectral features can change, altering both the isotropic and dichroic spectra. Alternatively, of more importance for small parameters, a parameter can change the nature of the ground state which can affect the final states that can be reached. Such an effect is already visible in the isotropic spectrum of divalent cobalt. From the degeneracies of the $2p_{3/2}$ and $2p_{1/2}$ core levels, one expects the intensity ratio of the L_3 and L_2 edges to be 2 in the absence of $3d$ spin-orbit interaction, assuming the core-valence electrostatic interaction is small compared to the (final state) core level $2p$ spin-orbit interaction. However, a finite spin-orbit coupling in the ground state drastically changes the spectral line shape and increases the L_3-L_2 branching ratio even when the final states are identical [55,56,66]. This phenomenon also underlies the changes in the x-ray linear dichroism due to a trigonal distortion. Since the trigonal distortion is expected to be of the order of a few tens of meV, its effect on the final states is expected to be small. However, the distortion more strongly affects the ground state, which changes how the final states are accessed via the dipole selection rules. For a trigonal distortion, this predominantly affects the XLD.

Since the changes in the XLD are a result of the ground-state properties, they are also reflected in the sum rules that relate the integrated intensity of the spectra to ground-state expectation values of particular operators. By performing an integration over the spectral line shapes, all details of the final states are removed. However, since the spectral line shapes hardly change for small trigonal fields, see Fig. 3, the integrated intensity directly reflects the size of the XLD signal. The sum rules for normalized intensities are given by [57,60,64]

$$\frac{I^k}{I^0} = \frac{\langle \underline{w}_0^k \rangle}{\langle n_h \rangle}, \tag{2}$$

where I^k refers to the integrated intensity of the isotropic, circular dichroic, and linear dichroic spectra for $k = 0, 1, 2$, respectively. The hole operators are spherical tensors of rank k [60,67]. They are given by

$$\underline{w}_q^k = \sum_{mm'\sigma} \underline{w}_{q,m'm}^k c_{m'\sigma} c_{m\sigma}^{\dagger},$$

where $c_{m\sigma}^{\dagger}$ creates an electron in a d orbital with projected angular momentum m and spin $\sigma = \pm\frac{1}{2}$. The coefficients can be written in terms of $3j$ symbols,

$$\underline{w}_{q,m'm}^k = (-1)^{l-m'} \begin{pmatrix} l & k & l \\ -m' & q & m \end{pmatrix} \Big/ \begin{pmatrix} l & k & l \\ -l & 0 & l \end{pmatrix}. \tag{3}$$

The angular momentum for d electrons is $l = 2$ with the projected angular momentum $m = 2, 1, 0, -1, -2$. For $k = 0$

(isotropic spectra), the coefficients $\underline{w}^0_{0,m'm} = \delta_{mm'}$ and the operator is $\underline{w}^0 = n_h$, where n_h is the number of holes in the valence shell (the $3d$ orbitals for Co^{2+}). The integrated intensity of the isotropic spectra is therefore simply proportional to the number of holes in the $3d$ orbitals. For circular dichroism, with $k = 1$ and $q = 0$, the coefficients are $\underline{w}^1_{0,m'm} = (m/l)\delta_{mm'}$. Therefore, $\underline{w}^1_0 = L_z/l$ is the orbital angular momentum of the empty states with $l = 2$ for transition metals. Generally, $\underline{w}^1_q = L_q/l$, where L_q is the angular momentum written in spherical coordinates. The integrated intensity of the XMCD is therefore proportional to the orbital angular momentum, which is a well-known sum rule [57].

Our interest lies in $\underline{w}^2$ which is related to quadrupole moment of the holes in the d orbital. For atomic orbitals, $\underline{w}^2$ is diagonal with matrix elements $(\underline{w}^2_0)_{mm} = \frac{1}{2}m^2 - 1$ giving $-1, -\frac{1}{2}, 1$ for $|m| = 0, 1, 2$. Therefore, the quadrupole moment increases when the orbital lies more in the xy plane. The same holds when writing the quadrupole moment in a real or tesseral basis with $(\underline{w}^2_0)_{\mu\mu} = \frac{1}{2}\mu^2 - 1$ with $\mu = 2, 1, 0, -1, -2 = x^2-y^2, zx, 3z^2-r^2, yz, xy$. Note that the tesseral index μ reflects the atomic orbitals $m = \pm|\mu|$ that the real orbitals are composed of.

Although the preceding works well for a tetragonal distortion where the z axis of the octahedron is elongated, the situation for a trigonal distortion is more complex. The distortion occurs in the (111) direction and the real orbitals are no longer eigenstates of the crystal field. Additionally, the measurements are performed near the (111) direction of the octahedron. To take the direction into account, we have to orient the quadrupole operator,

$$w^k_0(\theta, \varphi) = \mathbf{C}^k(\theta, \varphi) \cdot \mathbf{w}^k = \sum_{q=-k}^{k} (-1)^q C^k_{-q}(\theta, \varphi) w^k_q, \quad (4)$$

where $C^k_q(\theta, \varphi) = \sqrt{4\pi/(2k+1)}Y_{kq}(\theta, \varphi)$ is a renormalized spherical harmonic. For many experiments, the z direction ($\theta = 0$) is the reference axis and $w^k_0(0, \varphi) = \mathbf{C}^k(0, \varphi) \cdot \mathbf{w}^k = C^k_0(0, \varphi)w^k_0 = w^k_0$ using $C^k_q(0, \varphi) = \delta_{q,0}$. (Note that here θ is conventional spherical coordinate notation in the local octahedral frame, not to be confused with the incidence angle in experimental geometry shown in Fig. 1). This reduces to the results above, since the w^k_q were defined with respect to the z axis. For the (111) direction, we have for the quadrupole $w^k_{(111)} \equiv w^k_0(\arccos(1/\sqrt{3}), \frac{\pi}{4})$, where (111) indicates the new reference axis, i.e., the new z axis of the system. Additionally, it is more convenient to use a trigonal basis for the t_{2g} orbitals [43],

$$|0_{\text{eff}}\rangle = \frac{1}{\sqrt{3}}(|yz\rangle + |zx\rangle + |xy\rangle), \quad (5)$$

$$|\pm 1_{\text{eff}}\rangle = \pm\frac{1}{\sqrt{3}}(e^{\pm i\frac{2\pi}{3}}|yz\rangle + e^{\mp i\frac{2\pi}{3}}|zx\rangle + |xy\rangle). \quad (6)$$

Within this basis, the quadrupole moment can be written in matrix form as

$$w^2_{(111)} = \frac{1}{2}\left(\begin{array}{ccc|cc} 0 & 0 & i & 0 & i \\ 0 & 0 & 1 & 0 & -1 \\ -i & 1 & 1 & 0 & 0 \\ 0 & 0 & 0 & -2 & 0 \\ -i & 1 & 0 & 0 & 1 \end{array}\right) \begin{array}{l} x^2-y^2\,(e_g) \\ 3z^2-r^2\,(e_g) \\ 1_{\text{eff}}\,(e_g) \\ 0_{\text{eff}}\,(a_{1g}) \\ -1_{\text{eff}}\,(e_g) \end{array}, \quad (7)$$

where the basis of the matrix is indicated on the right; e_g and a_{1g} denote the symmetry in Mulliken notation. It is intuitive to split the action of the quadrupole operator for the e_g and t_{2g} orbitals. The diagonal components for the e_g orbital are zero. They are finite for the t_{2g} orbitals and the diagonal terms are equivalent to half times the quadrupole operator w^2_0 of a p orbital ($l_{\text{eff}} = 1$) with $\frac{1}{2}w^2_0 = \frac{3}{2}(m^2_{\text{eff}} - \frac{2}{3})$. Additionally, they are, apart from a scaling, equivalent to the trigonal distortion in the trigonal basis,

$$H_{\text{trig}} = \sum_{\sigma=\pm\frac{1}{2}} \sum_{m_{\text{eff}}=-1}^{1} \Delta\left(m^2_{\text{eff}} - \frac{2}{3}\right)c_{m_{\text{eff}}\sigma}c^\dagger_{m_{\text{eff}}\sigma}, \quad (8)$$

where for $\Delta > 0$, the holes preferentially go into the $m_{\text{eff}} = 0$ (a_1) state.

Therefore, since the XLD is related to the quadrupole moment, it is also a direct measure of the trigonal distortion. Although this describes well the trends of the XLD, the off-diagonal matrix elements in Eq. (7) and many-body effects complicate the interpretation, as we shall see below.

D. Ground state

The lowest energy states of divalent cobalt are relatively complex. The starting point is a high-spin state stabilized by the dd Coulomb interaction and the octahedral crystal field; see Fig. 4(top). This 12-fold degenerate state is then split by the spin-orbit interaction. These states are then further mixed and split by the trigonal field. The lowest twelve eigenenergies are plotted as a function of the trigonal crystal field, see Eq. (8), in Fig. 4(bottom). When including all interactions, all eigenstates are twofold degenerate. The other eigenstates are separated by close to an eV or more in energy due to the octahedral crystal field and the dd Coulomb interaction.

The high-spin ground state for Co^{2+} including only the Coulomb interaction and the octahedral crystal field is $^4T_1$ with a predominantly $t_{2g}e^2_g(^3A_2)$ configuration in hole notation. For the e_g holes and $S_z = S = 1$, e^2_g with $^3A_2$ symmetry implies a $x^2-y^2\uparrow, 3z^2-r^2\uparrow$ configuration. This is then coupled to a hole in a t_{2g} orbital giving a irreducible representation $A_2 \otimes T_2 = T_1$. For the high-spin ground state favored by the Coulomb interaction the total spin is $S = \frac{3}{2}$ leading to a quartet state ($2S + 1 = 4$). The orbital part of the coupled ground state, T_1, can again be interpreted in terms of an effective orbital angular momentum $L_{\text{eff}} = 1$ with projection $M_{\text{eff}} = 1, 0, -1$. Since the $e^2_g(^3A_2)$ configuration has no effective orbital angular momentum, M_{eff} is entirely determined by the m_{eff} of the t_{2g} or $l_{\text{eff}} = 1$ orbital for this configuration.

The 12-fold degenerate $^4T_1$ is split by the spin-orbit interactions. The splitting is seen for $\Delta = 0$ in Fig. 4(bottom). The trends can be rather well understood using an L_{eff} model [43]. The spin-orbit interaction $\zeta'\mathbf{L}_{\text{eff}} \cdot \mathbf{S}$ couples the angular momentum and the spin to a total angular momentum $\mathbf{J}_{\text{eff}}$. Although the agreement is good for $J_{\text{eff}} = \frac{1}{2}, \frac{3}{2}$, discrepancies occur for $J_{\text{eff}} = \frac{5}{2}$, which is split in the many-body calculation due to interactions with higher-lying multiplets. This is to be expected from symmetry arguments. The smaller J_{eff} values do not split $\frac{1}{2} \to E'$ and $\frac{3}{2} \to U'$ when going from effective spherical symmetry to octahedral irreducible
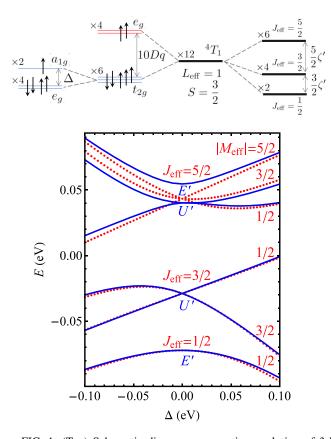
FIG. 4. (Top) Schematic diagram representing evolution of $3d$ states under the consecutive actions of octahedral and trigonal ($\Delta > 0$) crystal fields (left side) and spin-orbit interaction with effective spin-orbit coupling ζ' (right side). (Bottom) The lowest 12 eigenenergies for Co^{2+} under the combined action of spin-orbit and trigonal field Δ (all energies are twofold degenerate). The solid lines give the result from the many-body calculation for the divalent cobalt ion. The dotted curves are obtained using an L_{eff} model for the many-body states. The labels in the center are only valid for $\Delta = 0$. The $J_{\mathrm{eff}} = \frac{1}{2}, \frac{3}{2}$ correspond to the irreducible representations E' and U', which are twofold and fourfold degenerate, respectively. Additional octahedral crystal-field effects split the $J_{\mathrm{eff}} = \frac{5}{2}$ into E' and U'. The trigonal crystal field further splits the states, which can be, approximately, indicated by the $|M_{\mathrm{eff}}|$ value.

representations [68]. However, the highest values $J_{\mathrm{eff}} = \frac{5}{2} \rightarrow U' \oplus E'$ are expected to split when lowering the symmetry from spherical to octahedral.

Note that the coupling strength for the many-body states is not the same as for the single-particle interaction. The effective spin-orbit interaction strength is $\zeta' \cong \alpha\zeta = 29$ meV with $\alpha \cong 0.44$. The eigenenergies for $J_{\mathrm{eff}} = \frac{1}{2}, \frac{3}{2}, \frac{5}{2}$ are $-\frac{5}{2}\zeta', -\zeta', \frac{3}{2}\zeta' = -72, -29, 43$ meV, respectively. The first excited state is $\frac{3}{2}\zeta' = 43$ meV higher in energy. The underlying reason is that the coupled L_{eff} and S produce the correct relative splitting, but the absolute energy separation requires the correct reduced matrix element. This is comparable to the Wigner-Eckart theorem. The relative splitting is given by $\langle J_{\mathrm{eff}}M_{\mathrm{eff}}|\mathbf{L}_{\mathrm{eff}} \cdot \mathbf{S}|J_{\mathrm{eff}}M_{\mathrm{eff}}\rangle = \frac{1}{2}[J_{\mathrm{eff}}(J_{\mathrm{eff}}+1) - L_{\mathrm{eff}}(L_{\mathrm{eff}}+1) - S(S+1)] = -\frac{5}{2}, -1, \frac{3}{2}$ for $J_{\mathrm{eff}} = \frac{1}{2}, \frac{3}{2}, \frac{5}{2}$ with $L_{\mathrm{eff}} = 1$ and $S = \frac{3}{2}$. However, the expectation value of the one-particle spin-orbit interaction is given

by $\langle J_{\mathrm{eff}}M_{\mathrm{eff}}|\zeta \sum_i \mathbf{l}_i \cdot \mathbf{s}_i|J_{\mathrm{eff}}M_{\mathrm{eff}}\rangle = -\frac{5}{2}\zeta', -\zeta', \frac{3}{2}\zeta'$, where the summation goes over the electrons in the $3d$ shell and $\zeta' = \alpha\zeta$ is effective spin-orbit coupling strength.

Let us try to get a better understanding of the reduced matrix element. To lowest order the expected Hund's rule ground state in octahedral symmetry is $^4T_1(t_{2g}e_g^2(^3A_2))$. Note that there is a single hole in the t_{2g} states. In analogy to the iridates, one might expect the t_{2g} states to split into an effective $j_{\mathrm{eff}} = \frac{1}{2}, \frac{3}{2}$ under the spin-orbit interaction. The hole would then preferentially go into the $j_{\mathrm{eff}} = \frac{1}{2}$ state. Although this tendency is there, the Coulomb interaction and the crystal field impose the $^4T_1$ state and the spin of the t_{2g} hole has to be coupled parallel to the $S = 1$ spin of the e_g^2 holes. The result is that, for $J_{\mathrm{eff}} = \frac{1}{2}$, the ratio of $j_{\mathrm{eff}} = \frac{1}{2}$ to $j_{\mathrm{eff}} = \frac{3}{2}$ character of the t_{2g} hole is $8 : 1$. This demonstrates that the many-body $J_{\mathrm{eff}} = \frac{1}{2}$ state does not simply have a high-spin hole configuration of $t_{2g\uparrow}e_{g\uparrow}^2$ with the t_{2g} hole in the $j_{\mathrm{eff}} = \frac{1}{2}$ state. For the $J_{\mathrm{eff}} = \frac{3}{2}$, the ratio is $5 : 4$, whereas the $J_{\mathrm{eff}} = \frac{5}{2}$ is composed solely of $j_{\mathrm{eff}} = \frac{3}{2}$ holes.

From the ratios of j_{eff} character, the expectation value of the spin-orbit interaction can be calculated giving, for $J_{\mathrm{eff}} = \frac{1}{2}$, $\langle \mathbf{l} \cdot \mathbf{s} \rangle = \frac{8}{9}(-1) + \frac{1}{9}\frac{1}{2} = -\frac{5}{6}$ using that $\mathbf{l} \cdot \mathbf{s} = -1, \frac{1}{2}$ for $j_{\mathrm{eff}} = \frac{1}{2}, \frac{3}{2}$, respectively. For $J_{\mathrm{eff}} = \frac{3}{2}$, one finds $\langle \mathbf{l} \cdot \mathbf{s} \rangle = \frac{5}{9}(-1) + \frac{4}{9}\frac{1}{2} = -\frac{1}{3}$. Since the $J_{\mathrm{eff}} = \frac{5}{2}$ only contains $j_{\mathrm{eff}} = \frac{3}{2}$, its spin-orbit coupling is $\langle \mathbf{l} \cdot \mathbf{s} \rangle = \frac{1}{2}$. Therefore, the reduced matrix element is $\alpha = \frac{1}{3} \cong 0.33$. Note that the spin-orbit coupling is entirely determined by the hole in the t_{2g} states and therefore does not exceed the range $[-1, \frac{1}{2}]$.

However, this is not the entire story since numerically it was found that $\alpha \cong 0.44$. The reason for the larger value is that $^4T_1(t_{2g}e_g^2(^3A_2))$ is not the only $^4T_1$ state. The Coulomb interaction couples this state to $^4T_1(t_{2g}^2(^3T_1)e_g)$. Neglecting the spin-orbit interaction, this coupling can be calculated from

$$H = \begin{pmatrix} -12B & 6B \\ 6B & 10Dq - 3B \end{pmatrix} \begin{array}{l} {}^4T_1(t_{2g}e_g^2(^3A_2)) \\ {}^4T_1(t_{2g}^2(^3T_1)e_g) \end{array}, \qquad (9)$$

where the configurations are given on the right. The Coulomb coupling is given by the Racah parameter $B = 0.109$ eV. With $10Dq = 1.1$ eV, this gives about 8% $^4T_1(t_{2g}^2(^3T_1)e_g)$ character in the ground state. The increased hole density in the t_{2g} orbitals plus the additional spin-orbit coupling between the t_{2g} and e_g holes gives $\alpha \cong 0.47$. The expectation values of the spin-orbit coupling are then $\langle ^4T_{1J_{\mathrm{eff}}}| \sum_i \mathbf{l}_i \cdot \mathbf{s}_i|^4T_{1J_{\mathrm{eff}}}\rangle = -\frac{5}{2}\alpha, -\alpha, \frac{3}{2}\alpha = -1.19, -0.47, 0.71$ for $J_{\mathrm{eff}} = \frac{1}{2}, \frac{3}{2}, \frac{5}{2}$ for the lowest quartet states. A full many-body calculation using all the configurations gives, in the absence of a trigonal crystal field, $\langle ^4T_{1J_{\mathrm{eff}}}| \sum_i \mathbf{l}_i \cdot \mathbf{s}_i|^4T_{1J_{\mathrm{eff}}}\rangle = -1.34, -0.74$ for $J_{\mathrm{eff}} = \frac{1}{2}, \frac{3}{2}$. The $J_{\mathrm{eff}} = \frac{5}{2}$ is split under the octahedral crystal field giving expectation values of 0.17 and 0.61 for E' and U', respectively.

The ground-state expectation value can be used to estimate the isotropic branching ratio, i.e., the ratio $BR = I_{L_3}/I_{L_2}$ of the integrated intensities of the L_3 and L_2 edges [55,56,64,66]. As can be seen from Fig. 2, the branching ratio deviates strongly from the expected $2 : 1$ ratio based on the degeneracy of the $2p_j$ core levels. The branching ratio is $BR = (2 + r)/(1 - r)$ where $r = -\langle ^4T_{1\frac{1}{2}}| \sum_i \mathbf{l}_i \cdot \mathbf{s}_i|^4T_{1\frac{1}{2}}\rangle/n_h$, where $n_h = 3$ is the

number of holes. Inserting the values gives BR = 4.42. The branching ratio of the calculated spectrum is BR = 4.86. The difference occurs because the sum rule assumes that the j value of the core level is a good quantum number. In reality, the two edges are mixed, predominantly due to Coulomb interactions. Calculating the spectra from excited J_{eff} values gives strongly different branching ratios even though the final states are equivalent. The change in branching ratio is therefore not a result of the change in the final states, but what final states can be accessed starting from a particular ground state. This is also important for the trigonal crystal field, which changes what final states are accessed even though the trigonal field is so small that it barely affects the x-ray absorption final states.

E. Trends in quadrupole moment

Up to this point, we have seen that the introduction of a trigonal field gives rise to an XLD signal. Good agreement with the experimental TFY data ($T = 2$ K) can be found for $\Delta \cong 35$ meV (Fig. 3). It should be noted that the size of the signal can be rather sensitive to the experimental conditions and measurement technique. Data obtained in TEY mode ($T = 150$ K), see Appendix, gives a signal with the same sign but larger intensity, yielding $\Delta \cong 60$ meV. The integrated intensity of the XLD is proportional to the quadrupole moment, which can be related to the trigonal field. Since the shape of the XLD spectrum is hardly affected by the small trigonal field, the quadrupole moment effectively gives the size of the XLD signal. We now would like to understand the trend of the quadrupole moment (or, equivalently, the size of the trigonal field) and hence the size of the XLD as a function of the trigonal field parameter Δ. The coupled $J_{eff}M_{eff}$ values are used to describe the trends. From the discussion of the spin-orbit coupling, we know that the coupled angular momenta can provide a good idea of the splitting, but a reduced matrix element is needed to relate it to the microscopic value. We focus on the trend and obtain the reduced matrix element numerically. The trigonal field in the coupled $L_{eff}M_{eff}$ basis is $H_{trig} = \frac{2}{3}\Delta W^2 = \Delta(M_{eff}^2 - \frac{2}{3})$, see Eq. (8), where W^2 is the quadrupole moment due to the t_{2g} orbitals from Eq. (7) in the coupled basis. Within the lowest configuration $^4T_1$, $\zeta' \mathbf{L}_{eff} \cdot \mathbf{S}$ is the dominant interaction. It is therefore advantageous to write the Hamiltonian in the coupled $|J_{eff}M_{eff}\rangle$ basis. In this basis, the spin-orbit interaction becomes diagonal,

$$H_{SOI} = \zeta' \begin{pmatrix} -\frac{5}{2} & 0 & 0 \\ 0 & -1 & 0 \\ 0 & 0 & \frac{3}{2} \end{pmatrix} \begin{matrix} J_{eff}, |M_{eff}| = \frac{1}{2}, \frac{1}{2} \\ \frac{3}{2}, \frac{1}{2} \\ \frac{5}{2}, \frac{1}{2} \end{matrix}. \quad (10)$$

Note that M_{eff} is also a good quantum number, and we can focus on $|M_{eff}| = \frac{1}{2}$. The trigonal field, which was diagonal in the uncoupled basis, $|L_{eff}M_{eff}, SM_S\rangle$ with $L_{eff} = 1$ and $S = \frac{3}{2}$, now becomes off-diagonal,

$$H_{trig} = \Delta \begin{pmatrix} 0 & -\frac{1}{3\sqrt{5}} & \frac{1}{\sqrt{5}} \\ -\frac{1}{3\sqrt{5}} & \frac{4}{15} & \frac{1}{5} \\ \frac{1}{\sqrt{5}} & \frac{1}{5} & -\frac{4}{15} \end{pmatrix} \begin{matrix} J_{eff}, |M_{eff}| = \frac{1}{2}, \frac{1}{2} \\ \frac{3}{2}, \frac{1}{2} \\ \frac{5}{2}, \frac{1}{2} \end{matrix}.$$
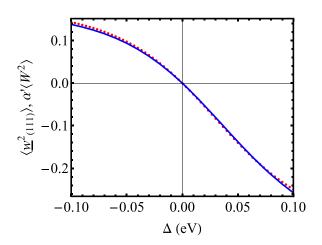

FIG. 5. Comparison between the expectation value of the microscopic quadrupole moment $\langle w^2 \rangle$ (blue) and the scaled quadrupole moment $\alpha'\langle W^2 \rangle$ for the coupled basis (red dotted).

The eigenvalues E_n and eigenstates $|E_n\rangle$ with $n = 0, 1, 2$ of $M_{eff} = \frac{1}{2}$ can be found by diagonalizing the total Hamiltonian for $|M_{eff}| = \frac{1}{2}$, $H = H_{SOI} + H_{trig}$. In the limit $\Delta \ll \zeta'$, the energy of the ground state $|E_0\rangle$ can be approximated by

$$E_0 = -\frac{5}{2}\zeta' - \frac{\Delta^2}{45\left(\frac{3}{2}\zeta' + \frac{4}{15}\Delta\right)} - \frac{\Delta^2}{5\left(4\zeta' - \frac{4}{15}\Delta\right)}. \quad (11)$$

This approximates the parabolic behavior for small Δ of the lowest curve in Fig. 4. Note that the change in energy is proportional to $-\sum_{i=2,3} H_{1,i}^2/(H_{i,i} - H_{1,1})$, where $H_{i,j}$ with $i, j = 1, 2, 3$ is a matrix element in the total Hamiltonian.

Note that the mixing of the $J_{eff} = \frac{1}{2}$ state with the other $J_{eff} = \frac{3}{2}, \frac{5}{2}$ is relatively small, of the order of 3%–8% for $\Delta = 35$–60 meV. This is because the mixing is proportional to $[H_{1,i}/(H_{i,i} - H_{1,1})]^2$ which is small. Since the spin-orbit interaction is diagonal, this barely affects the ground-state expectation value of the spin-orbit interaction, giving a relatively pure $J_{eff} = \frac{1}{2}$ state. However, it affects more strongly the expectation value of the trigonal field (and the related quadrupole moment) which is proportional to $H_{1,i}/(H_{i,i} - H_{1,1})$ due to the off-diagonal terms between the $J_{eff} = \frac{1}{2}$ and the $J_{eff} = \frac{3}{2}, \frac{5}{2}$.

The trends in the quadrupole moment are given by $\langle W^2 \rangle = \frac{3}{2}\langle E_0|H_{trig}|E_0\rangle/\Delta$, which is directly proportional to the ground-state expectation value of the trigonal field. As for the spin-orbit coupling, the value of W^2 overestimates the magnitude of the expectation value $\langle w_{(111)}^2 \rangle$ from Eq. (7) in the many-body ground state. The expectation value of $\langle W^2 \rangle$ is therefore scaled down by its reduced matrix element $\alpha' = 0.38$.

Figure 5 shows a comparison between the microscopic quadrupole moment $\langle w_{(111)}^2 \rangle$ and the scaled quadrupole moment $\alpha'\langle W^2 \rangle$ for the coupled basis. As is clear, there is a good agreement for the trends from the coupled basis. From the sum rules we know that the expectation values directly reflect the XLD signal. Therefore, the XLD is directly proportional to the size of the change in ground-state energy due to the trigonal field. A change in the sign of the trigonal field therefore causes a change in sign of the XLD signal. These trends are

in agreement with the calculation in Fig. 3. Although the size of the XLD increases with Δ, the magnitude is not entirely symmetric for positive and negative Δ.

Whereas $\langle \underline{w}^2_{(111)} \rangle = \alpha' \langle W^2 \rangle$ is relevant for the integrated intensity of the XLD spectrum, the expectation values can also be related to the hole densities in the ground state. The hole density in the a_{1g} orbital is given by $\underline{n}_{a_{1g}} = -\langle W^2 \rangle + \frac{1}{3}$. This gives $\underline{n}_{a_{1g}} = 0.59$–$0.77$ for $\Delta = 35$–60 meV. The trigonal field does not directly lead to a hole in the a_{1g} orbital as one might expect from a simple independent-particle level scheme.

F. XMCD

The XMCD data, see Fig. 2(g), are sensitive to the magnetic moment. Sum rules [57,58] allow us to relate the integrated intensities of the XMCD to the expectation values of the orbital (L_z) and spin (S_z) angular momentum. Alternatively, since the experimental spectra can be satisfactorily reproduced theoretically, the expectation values can also be calculated. Numerically, the expectation values are found to be $\langle L_z \rangle = -0.57$ and $\langle S_z \rangle = -0.83$ in units of $\hbar$ for a trigonal field of 35 meV. The values are rather insensitive to the trigonal field, yielding $\langle L_z \rangle = -0.57$ and $\langle S_z \rangle = -0.84$ when increasing the field to 60 meV.

Experimentally, the expectation values can be deduced from the spectral line shape using the sum rules [57,58]; see Fig. 8. Having the numerical calculations of the spectral line shape and the expectation values allows us to check the validity of the sum rules. Numerically, the sum rule reproduces the value for L_z, since this sum rule is exact. Discrepancies can be found when using the S_z sum rule. There are two assumptions in the use of the S_z sum rule. First, the sum rule also contains a magnetic dipole operator, which is generally assumed to be small. Numerically, it is found that $|\langle T_z \rangle| < 0.003$, so this assumption is justified. Second, the derivation of the S_z sum rule [58] assumes that each spin-orbit split edge can be described by the j value of the $2p$ core hole. This is generally a good assumption for late transition metal ions where there is less mixing of the spin-orbit split edges by the Coulomb interaction. The value of projected spin from the calculated spectra is $\langle S_z \rangle = -0.82$. The value differs by only 1.2% from the calculated expectation values. Therefore, the sum rules work well for divalent cobalt.

Applying the sum rules to the experimental spectra gives $\langle L_z \rangle = -0.61$ and $\langle S_z \rangle = -0.59$. The value for $\langle L_z \rangle$ agrees well with the theoretical value, whereas a smaller value is found for S_z. The major source of the discrepancy is the size of the XMCD signal at the L_2 edge, which is smaller in the experimental spectra. This increases the value of L_z, but decreases S_z. Both experimental and theoretical S_z values are significantly smaller than the value of $\langle S_z \rangle = -\frac{3}{2}$ that one might naively expect from a spin-only, high-spin $^4T_1$ state.

The experimental (theoretical) value of the projection of magnetic moment along applied field, $M_z = -(\langle L_z \rangle + 2\langle S_z \rangle)\mu_B/\hbar$, is 1.79 (2.23) μ_B. These values are in reasonable agreement with results from magnetometry of 2.25 μ_B/Co at 6 T [48], 2.1 μ_B/Co at 9 T [47], and 2.0 μ_B/Co at 5 T [46]. Using the relation $M_z = g M_{J_{\text{eff}}}$ with $M_{J_{\text{eff}}} = \frac{1}{2}$ one derives effective g factors of 3.58 and 4.46 from experiment and theory, respectively. Although these effective g values are for a

powder average, it is interesting to compare these values with anisotropic g_{ab}, g_c factors derived from analysis of magnetic susceptibility data [43], $g_{ab} \sim 4.6$ and $g_c \sim 3$. Interestingly, a powder average of these anisotropic g factors yields $g \sim 4$, which is close to the effective g value obtained from our data and theoretical analysis.

While the ground-state magnetic structure of $Na_3Co_2SbO_6$ is well known to be zigzag with propagation vector $(0.5,0.5,0)$ [47,48], less is known about the magnetic structure in applied field. Recent neutron diffraction work [69] shows that in-plane fields as low as 0.5–0.8 T drive a new magnetic structure with a $(1/3, 1/3, 1/3)$ propagation vector, presumably a ferrimagnetic state, and that no AFM order is seen above 2.2 T. In a separate study, a H-T phase diagram derived from ^{23}Na NMR, specific heat, and magnetometry reveals a saturated magnetization region at low T and high fields above about 3 T [70], consistent with previous magnetometry measurements [46–48]. The 14 T applied field used in the XMCD measurements ($T = 2$ K) places the system in the field-induced "saturation" region of the phase diagram in Ref. [70]. Whether the field-induced state at 14 T is fully polarized with Co moments aligned along the applied field remains to be determined. However, the fact that the magnetic moment per Co ion obtained from magnetometry is very close to the local-moment values derived from single-ion numerical calculations that reproduce the XMCD data indicates that the in-field 14 T state is close to a fully polarized state as the net moment per Co ion approaches the local moment.

IV. CONCLUSIONS

In this paper, x-ray dichroic experiments have been presented for a potential Kitaev QSL material. The divalent cobalt ion is in a high-spin $(^4T_1)$ state. Under the spin-orbit interaction, these states are split into an effective total angular momentum $J_{\text{eff}} = \frac{1}{2}, \frac{3}{2}, \frac{5}{2}$. X-ray spectroscopy clearly confirms that the ground state has predominantly $J_{\text{eff}} = \frac{1}{2}$ character (or the E' irreducible representation). This manifests itself by a large branching ratio in the isotropic and circular dichroic absorption spectra.

Although the calculations are done with an atomic $3d$ spin-orbit interaction strength of $\zeta = 66$ meV, the effective coupling strength for the J_{eff} many-body states is $\zeta' = 29$ meV. This agrees with the value of 30 meV taken by Liu et al. [43] and the 27–28 meV values derived from inelastic neutron scattering data [53,54]. Since the spin-orbit split manifolds are close in energy, they can be relatively easily mixed even by a weak perturbation such as the trigonal field. The changes in the ground state due to the trigonal field are studied using XLD. Analysis of the spectral line shapes allows us to confirm a positive trigonal field in the range 35–60 meV leading to an enhanced hole density in the a_{1g} orbital. Although the derived magnitude of the crystal field has significant errors due to differences in bulk-sensitive (TFY) and surface-sensitive (TEY) data, the positive sign of the trigonal field is a robust result. A positive sign is also found from modeling of crystal field excitations in inelastic neutron scattering data [53]. Therefore, despite the compression of the octahedra along their trigonal axis, a positive value of the trigonal field is found. The range of values agrees with

$\Delta = 38$ meV found by Liu *et al.* [43] from susceptibility measurements, although a smaller value of $\Delta = 12$ meV was derived from modeling of crystal field excitations in inelastic neutron scattering data [53].

The rather small and comparable energy scales of spin-orbit interaction and trigonal crystal field leads to a rather complex ground state. The ground state of Co^{2+} in the absence of spin-orbit coupling and trigonal crystal field has a hole configuration $t_{2g}e_g^2$. When switching on the spin-orbit interaction, one might expect that, in analogy to the iridates, the hole goes into the $j_{eff} = \frac{1}{2}$ formed by coupling the spin and the orbital angular momentum of the t_{2g} hole. However, although the trend is there, the situation is more complex since $^4T_1$ is a many-body state stabilized by the Coulomb interaction. One therefore finds an admixture of $j_{eff} = \frac{3}{2}$ hole density even for a zero trigonal field. Likewise, switching on the trigonal field does not directly lead to a hole in the a_{1g} state, but to an increased density in the a_{1g} state of 0.59–0.77 holes for a trigonal field of 35–60 meV. Even though the trigonal field increases the mixing of the $J_{eff} = \frac{1}{2}$ with the $J_{eff} = \frac{3}{2}, \frac{5}{2}$ states, the ground state still has predominately $J_{eff} = \frac{1}{2}$ character, amounting to over 90% of the $J_{eff} = \frac{1}{2}$ character of the ground state for the case of zero trigonal field.

In summary, the results provide experimental validation of the (counterintuitive) positive sign of the trigonal crystal field acting on Co^{2+} ions, bracket the magnitude of the trigonal crystal field, and validate the $J_{eff} = \frac{1}{2}$ description of the electronic ground state of $Na_3Co_2SbO_6$. In addition to providing independent confirmation of derivations based on magnetic susceptibility data [43,44] and inelastic neutron scattering data [53,54], the results provide a good foundation for experiments aimed at manipulating crystal field and exchange interactions with uniaxial strain or applied pressure toward stabilizing Kitaev's QSL state in this and other honeycomb cobaltate lattices with spin-orbit entangled 3d states.

APPENDIX

Although the experimental and theoretical spectral XLD line shapes can be reasonably reconciled, details and the absolute magnitude of the dichroic signal can be sensitive
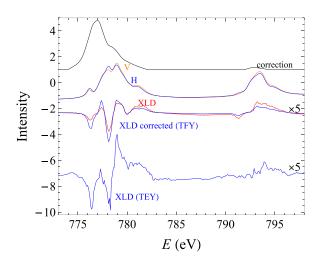

FIG. 6. The top black curve shows the scaling needed to make the isotropic TFY and TEY yields equal. The uncorrected spectra are shown in orange and blue for vertical (V) and horizontal (H) polarizations, respectively. The red and blue spectra show the XLD-TFY data before and after the self-absorption correction. The XLD-TFY is scaled by a factor 5. The bottom curve is the XLD-TEY data, scaled by a factor of 5.

to the experimental conditions and measurement techniques. The main text shows modeling of XLD data obtained using total fluorescence yield (TFY; $T = 2$–3 K). This detection technique is known to be affected by self-absorption effects, which reduce high intensities relative to low intensities. To correct for that, it was noted, based on modeling, that the sum of the TFY spectra measured in the horizontal and vertical polarization conditions is comparable to the isotropic spectrum measured in total electron yield (TEY) on
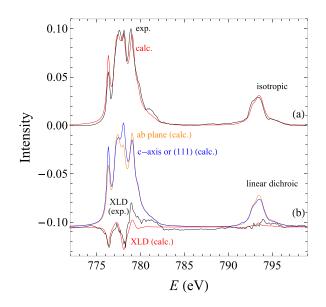

FIG. 7. Modeling of XLD data collected in TEY mode ($T = 150$ K). The figure shows the comparison between experimental (black) and calculated (red) spectra. (a) The isotropic spectra obtained by averaging both polarizations. (b) The x-ray linear dichroic spectrum, the difference of the spectra polarized in the *ab* plane and along the *c* axis. The *c* axis is approximately along the (111) direction of the CoO_6 octahedra.
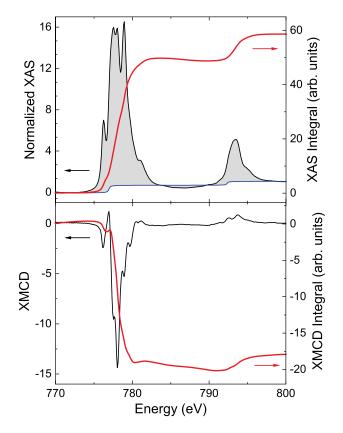
FIG. 8. Isotropic XAS (top) and XMCD (bottom) data collected on powder samples at 2 K in 14 T magnetic field, using TEY detection. Integrals used in sum rules analysis for derivation of expectation values of orbital, L_z, and spin, S_z, angular momentum are also shown. The isotropic spectra was used to obtain an *ad hoc* self-absorption correction to TFY data.

the powder sample (used for XMCD measurements). This is reasonable since the XLD signal is relatively small, and the TEY is not affected by self absorption. A small broadening is included to reduce the effects of experimental noise. After the correction, the TFY is again properly normalized. The results are shown in Fig. 6. The correction changes the relative intensities, but does not affect the overall XLD line shape. As expected, the XLD intensity at the L_3 edge is enhanced with respect to the L_2 edge.

Alternatively, TEY can be used to obtain the XLD spectra. TEY has the advantage that no self-absorption correction is needed. However, the data are more surface sensitive compared to TFY. There are two noticeable differences between the TEY ($T = 150$ K) and TFY ($T = 2$–3 K) data. First, the magnitude of the XLD is larger, requiring a trigonal field of 60 meV to explain the data. Second, although the main edge is satisfactorily explained, there is additional linear dichroism at the high-energy sides of both the L_3 and L_2 edges (Fig. 7). This intensity is not present in the TFY data and is not reproduced theoretically. We note that the TEY and TFY data were collected at different temperatures. Although the relatively low energy separation between ground and excited J_{eff} states may introduce temperature dependence in the XLD spectra, we did not carry out a systematic study of XLD as a function of temperature in this work.
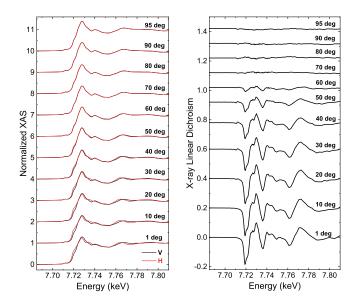

FIG. 9. Angular dependence of polarization-dependent XAS and computed XLD data at the Co K edge. Data were collected at $T = 2$ K in partial fluorescence yield mode. XLD vanishes when vertical and horizontal polarization lie in the honeycomb planes.

Figure 8 shows XAS and XMCD data collected on powder samples in TEY mode at $T = 2$ K, $H = 14$ T. Two arctan functions are used to mimic the absorption edge jumps at the Co $L_{2,3}$ edges. The widths of the arctan functions are set to the core-hole lifetimes of the respective edges, and their amplitude ratio set to 2:1, corresponding to the degeneracy of $2p_{3/2}$ and $2p_{1/2}$ core levels at L_3 and L_2 edges, respectively. After normalizing the XAS (and XMCD) data to edge jumps of 1:0.5 at these spin-orbit split edges, the integrals of the isotropic XAS fine structure (shaded area) and XMCD signals (red lines) were computed to derive the expectation values of L_z and S_z using sum rules analysis [57].

Figure 9 shows the angular dependence of Co K-edge XLD data collected in partial fluorescence yield mode ($T = 2$ K). In agreement with the angular evolution seen in the XLD of the
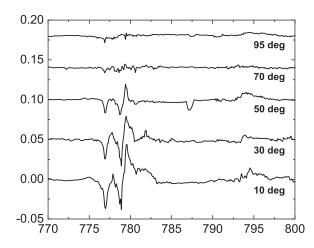

FIG. 10. Angle dependence of XLD data collected in TEY mode ($T = 150$ K). The XLD vanishes when both linear vertical and linear horizontal polarizations are in the honeycomb plane.

Co $L_{2,3}$ edges (Fig. 10), XLD is largest at grazing incidence and vanishes at normal incidence. Figure 10 shows the angular dependence of Co $L_{2,3}$ XLD data collected in TEY mode ($T = 150$ K).

[1] A. Kitaev, Ann. Phys. **321**, 2 (2006).

[2] M. Hermanns, I. Kimchi, and J. Knolle, Annu. Rev. Condens. Matter Phys. **9**, 17 (2018).

[3] H. Takagi, T. Takayama, G. Jackeli, G. Khaliullin, and S. Nagler, Nat. Rev. Phys. **1**, 264 (2019).

[4] A. Banerjee, C. Bridges, J.-Q. Yan, A. Aczel, L. Li, M. Stone, G. Granroth, M. Lumsden, Y. Yiu, S. Bhattacharjee *et al.*, Nat. Mater. **15**, 733 (2016).

[5] A. Banerjee, J.-Q. Yan, J. Knolle, C. Bridges, M. Stone, M. Lumsden, D. Mandrus, D. Tennant, R. Moessner, and S. Nagler, Science **356**, 1055 (2017).

[6] A. Banerjee, P. Lampen-Kelley, J. Knolle, C. Balz, A. Aczel, B. Winn, Y. Liu, D. Pajerowski, J. Yan, C. Bridges *et al.*, npj Quantum Mater. **3**, 8 (2018).

[7] R. Yadav, N. Bogdanov, V. M. Katukuri, S. Nishimoto, J. van der Brink, and L. Hozoi, Sci. Rep. **6**, 37925 (2016).

[8] S. Biswas, Y. Li, S. M. Winter, J. Knolle, and R. Valentí, Phys. Rev. Lett. **123**, 237201 (2019).

[9] J. Zheng, K. Ran, T. Li, J. Wang, P. Wang, B. Liu, Z.-X. Liu, B. Normand, J. Wen, and W. Yu, Phys. Rev. Lett. **119**, 227208 (2017).

[10] F. Bahrami, X. Hu, Y. Du, O. Lebedev, C. Wang, H. Luetkens, G. Fabbris, M. Graf, D. Haskel, Y. Ran *et al.*, Sci. Adv. **8**, eabl5671 (2022).

[11] P. Khuntia, S. Manni, F. R. Foronda, T. Lancaster, S. J. Blundell, P. Gegenwart, and M. Baenitz, Phys. Rev. B **96**, 094432 (2017).

[12] V. Katukuri, S. Nishimoto, I. Rousochatzakis, H. Stoll, J. van der Brink, and L. Hozoi, Sci. Rep. **5**, 14718 (2015).

[13] S. Chu, J.-W. Kim, J. Kim, H. Zheng, C. Stoumpos, C. Malliakas, J. Mitchell, K. Mehlawat, Y. Singh, Y. Choi *et al.*, Nat. Phys. **11**, 462 (2015).

[14] K. Kitagawa, T. Takayama, Y. Matsumoto, A. Kato, R. Takano, Y. Kishimoto, S. Bette, R. Dinnebier, G. Jackeli, and H. Takagi, Nature (London) **554**, 341 (2018).

[15] M. Abramchuk, C. Ozsoy-Keshinbora, J. Krizan, K. Metz, D. Bell, and F. Tafti, J. Am. Chem. Soc. **139**, 15371 (2017).

[16] T. Takayama, A. Kato, R. Dinnebier, J. Nuss, H. Kono, L. S. I. Veiga, G. Fabbris, D. Haskel, and H. Takagi, Phys. Rev. Lett. **114**, 077202 (2015).

[17] K. Modic, T. Smidt, I. Kimchi, N. P. Breznay, A. Biffin, S. Choi, R. D. Johnson, R. Coldea, P. Watkins-Curry, G. McCandless *et al.*, Nat. Commun. **5**, 4203 (2014).

[18] B. Kim, H. Ohsumi, T. Komesu, S. Sakai, T. Morita, H. Takagi, and T. Arima, Science **323**, 1329 (2009).

[19] B. J. Kim, H. Jin, S. J. Moon, J.-Y. Kim, B.-G. Park, C. S. Leem, J. Yu, T. W. Noh, C. Kim, S.-J. Oh, J.-H. Park, V. Durairaj, G. Cao, and E. Rotenberg, Phys. Rev. Lett. **101**, 076402 (2008).

[20] G. Jackeli and G. Khaliullin, Phys. Rev. Lett. **102**, 017205 (2009).

[21] X. Liu, T. Berlijn, W. G. Yin, W. Ku, A. Tsvelik, Y. J. Kim, H. Gretarsson, Y. Singh, P. Gegenwart, and J. P. Hill, Phys. Rev. B **83**, 220403(R) (2011).

[22] S. C. Williams, R. D. Johnson, F. Freund, S. Choi, A. Jesche, I. Kimchi, S. Manni, A. Bombardi, P. Manuel, P. Gegenwart, and R. Coldea, Phys. Rev. B **93**, 195158 (2016).

[23] F. Ye, S. Chi, H. Cao, B. C. Chakoumakos, J. Fernandez-Baca, R. Custelcean, T. F. Qi, O. Korneta, and G. Cao, Phys. Rev. B **85**, 180403 (R) (2012).

[24] A. Biffin, R. Johnson, S. Choi, F. Freund, S. Manni, A. Bombardi, P. Manuel, P. Gegenwart, and R. Coldea, Phys. Rev. B **90**, 205116 (2014).

[25] J. G. Rau, E. Kin-Ho Lee, and H.-Y. Kee, Phys. Rev. Lett. **112**, 077204 (2014).

[26] E. Kin-Ho Lee and Y. B. Kim, Phys. Rev. B **91**, 064407 (2015).

[27] G. Simutis, N. Barbero, K. Rolfs, P. Leroy-Calatayud, K. Mehlawat, R. Khasanov, H. Luetkens, E. Pomjakushina, Y. Singh, H.-R. Ott *et al.*, Phys. Rev. B **98**, 104421 (2018).

[28] K. Rolfs, S. Toth, E. Pomjakushina, D. Sheptyakov, J. Taylor, and K. Conder, Phys. Rev. B **91**, 180406(R) (2015).

[29] V. Hermann, J. Ebad-Allah, F. Freund, I. Pietsch, A. Jesche, A. Tsirlin, J. Deisenhofer, M. Hanfland, P. Gegenwart, and C. Kuntscher, Phys. Rev. B **96**, 195137 (2017).

[30] S. Manni, S. Choi, I. Mazin, R. Coldea, M. Altmeyer, H. Jeschke, R. Valenti, and P. Gegenwart, Phys. Rev. B **89**, 245113 (2014).

[31] H. Lei, W.-G. Yin, Z. Zhong, and H. Hosono, Phys. Rev. B **89**, 020409(R) (2014).

[32] M. Majumder, R. S. Manna, G. Simutis, J. C. Orain, T. Dey, F. Freund, A. Jesche, R. Khasanov, P. K. Biswas, E. Bykova, N. Dubrovinskaia, L. S. Dubrovinsky, R. Yadav, L. Hozoi, S. Nishimoto, A. A. Tsirlin, and P. Gegenwart, Phys. Rev. Lett. **120**, 237202 (2018).

[33] L. S. I. Veiga, M. Etter, K. Glazyrin, F. Sun, C. A. Escanhoela, G. Fabbris, J. R. L. Mardegan, P. S. Malavi, Y. Deng, P. P. Stavropoulos, H. Y. Kee, W. G. Yang, M. van Veenendaal, J. S. Schilling, T. Takayama, H. Takagi, and D. Haskel, Phys. Rev. B **96**, 140402(R) (2017).

[34] V. Hermann, M. Altmeyer, J. Ebad-Allah, F. Freund, A. Jesche, A. A. Tsirlin, M. Hanfland, P. Gegenwart, I. I. Mazin, D. I. Khomskii, R. Valenti, and C. A. Kuntscher, Phys. Rev. B **97**, 020104(R) (2018).

[35] V. Hermann, S. Biswas, J. Ebad-Allah, F. Freund, A. Jesche, A. A. Tsirlin, M. Hanfland, D. Khomskii, P. Gegenwart, R. Valenti, and C. A. Kuntscher, Phys. Rev. B **100**, 064105 (2019).

[36] G. Bastien, G. Garbarino, R. Yadav, F. J. Martinez-Casado, R. Beltran Rodriguez, Q. Stahl, M. Kusch, S. P. Limandri, R. Ray, P. Lampen-Kelley, D. G. Mandrus, S. E. Nagler, M. Roslova, A. Isaeva, T. Doert, L. Hozoi, A. U. B. Wolter, B. Buchner, J. Geck, and J. van den Brink, Phys. Rev. B **97**, 241108(R) (2018).

[37] L. S. I. Veiga, K. Glazyrin, G. Fabbris, C. D. Dashwood, J. G. Vale, H. Park, M. Etter, T. Irifune, S. Pascarelli, D. F. McMorrow, T. Takayama, H. Takagi, and D. Haskel, Phys. Rev. B **100**, 064104 (2019).

[38] B. Shen, A. Jesche, M. L. Seidler, F. Freund, P. Gegenwart, and A. Tsirlini, Phys. Rev. B **104**, 134426 (2021).

[39] J. P. Clancy, H. Gretarsson, J. Sears, Y. Singh, S. Desgreniers, K. Mehlawat, S. Layek, G. K. Rozenberg, Y. Ding, M. Upton *et al.*, npj Quantum Mater. **3**, 35 (2018).

[40] T. Takayama, A. Krajewska, A. S. Gibbs, A. N. Yaresko, H. Ishii, H. Yamaoka, K. Ishii, N. Hiraoka, N. P. Funnell, C. L. Bull, and H. Takagi, Phys. Rev. B **99**, 125127 (2019).

[41] J. Park, T.-Y. Tan, D. Adroja, A. Daoud-Aladine, S. Choi, D.-Y. Cho, S.-H. Lee, J. Kim, H. Sim, T. Morioka *et al.*, Sci. Rep. **6**, 25238 (2016).

[42] M. van Veenendaal and D. Haskel, Phys. Rev. B **105**, 214420 (2022).

[43] H. Liu, J. Chaloupka, and G. Khaliullin, Phys. Rev. Lett. **125**, 047201 (2020).

[44] H. Liu and G. Khaliullin, Phys. Rev. B **97**, 014407 (2018).

[45] R. Sano, Y. Kato, and Y. Motome, Phys. Rev. B **97**, 014408 (2018).

[46] L. Viciu, Q. Huang, E. Morosan, H. Zandbergen, N. Greenbaum, T. McQueen, and R. Cava, J. Solid State Chem. **180**, 1060 (2007).

[47] C. Wong, M. Avdeev, and C. Ling, J. Solid State Chem. **243**, 18 (2016).

[48] J.-Q. Yan, S. Okamoto, Y. Wu, Q. Zheng, H. D. Zhou, H. Cao, and M. A. McGuire, Phys. Rev. Mater. **3**, 074405 (2019).

[49] M. Stratan, I. Shukaev, T. Vasilchikova, A. Vasiliev, A. Korshunov, A. Kurbakov, V. Nalbandyan, and E. Zvereva, New J. Chem. **43**, 13545 (2019).

[50] B.-J. Yang and Y. B. Kim, Phys. Rev. B **82**, 085111 (2010).

[51] S. Bhattacharjee, S.-S. Lee, and Y. B. Kim, New J. Phys. **14**, 073015 (2012).

[52] D. Khomskii, K. Kugel, A. Sboychakov, and S. Streltsov, J. Exp. Theor. Phys. **122**, 484 (2016).

[53] C. Kim, J. Jeong, G. Kin, P. Park, T. Masuda, S. Asai, S. Itoh, H.-S. Kim, H. Zhou, J. Ma *et al.*, J. Phys.: Condens. Matter **34**, 045802 (2022).

[54] M. Songvilay, J. Robert, S. Petit, J. A. Rodriguez-Rivera, W. D. Ratcliff, F. Damay, V. Baledent, M. Jimenez-Ruiz, P. Lejay, E. Pachoud, A. Hadj-Azzem, V. Simonet, and C. Stock, Phys. Rev. B **102**, 224429 (2020).

[55] G. van der Laan and B. T. Thole, Phys. Rev. Lett. **60**, 1977 (1988).

[56] M. A. Laguna-Marco, D. Haskel, N. Souza-Neto, J. C. Lang, V. V. Krishnamurthy, S. Chikara, G. Cao, and M. van Veenendaal, Phys. Rev. Lett. **105**, 216407 (2010).

[57] B. T. Thole, P. Carra, F. Sette, and G. van der Laan, Phys. Rev. Lett. **68**, 1943 (1992).

[58] P. Carra, B. T. Thole, M. Altarelli, and X. Wang, Phys. Rev. Lett. **70**, 694 (1993).

[59] J. Stöhr, J. Electron Spectrosc. Relat. Phenom. **75**, 253 (1995).

[60] B. Thole, G. van der Laan, and M. Fabrizio, Phys. Rev. B **50**, 11466 (1994).

[61] J. P. Hannon, G. T. Trammell, M. Blume, and D. Gibbs, Phys. Rev. Lett. **61**, 1245 (1988).

[62] F. M. F. de Groot, J. C. Fuggle, B. T. Thole, and G. A. Sawatzky, Phys. Rev. B **42**, 5459 (1990).

[63] J. Fernández-Rodríguez, B. Toby, and M. van Veenendaal, J. Electron Spectrosc. Relat. Phenom. **202**, 81 (2015).

[64] M. van Veenendaal, *The Theory of Inelastic Scattering and Absorption of X-Rays* (Cambridge University Press, Cambridge, 2015).

[65] G. van der Laan, J. Zaanen, G. A. Sawatzky, R. Karnatak, and J.-M. Esteva, Phys. Rev. B **33**, 4253 (1986).

[66] D. Haskel, G. Fabbris, M. Zhernenkov, P. P. Kong, C. Q. Jin, G. Cao, and M. van Veenendaal, Phys. Rev. Lett. **109**, 027204 (2012).

[67] M. van Veenendaal, Eur. J. Phys. **32**, 947 (2011).

[68] J. S. Griffith, *The Theory of Transition-Metal Ions* (Cambridge University Press, Cambridge, 1961).

[69] X. Li, Y. Gu, Y. Chen, V. O. Garlea, K. Iida, K. Kamazawa, Y. Li, G. Deng, Q. Xiao, X. Zheng, Z. Ye, Y. Peng, I. A. Zaliznyak, J. M. Tranquada, and Y. Li, Phys. Rev. X **12**, 041024 (2022).

[70] E. Vavilova, T. Vasilchikova, A. Vasiliev, D. Mikhailova, V. Nalbandyan, E. Zvereva, and S. V. Streltsov, Phys. Rev. B **107**, 054411 (2023).